Visualizing the metazoan proliferation-terminal differentiation decision *in vivo*

Abraham Q. Kohrman,[1,7] Rebecca C. Adikes,[1,7] Michael A. Q. Martinez,[1] Nicholas J. Palmisano,[1] Jayson J. Smith,[1] Taylor N. Medwig-Kinney,[1] Mingwei Min,[2] Maria D. Sallee,[3] Ononnah B. Ahmed,[1] Nuri Kim,[1] Simeiyun Liu,[1,4] Robert D. Morabito,[1] Nicholas Weeks,[1] Qinyun Zhao,[1] Wan Zhang,[1] Jessica L. Feldman,[3] Michalis Barkoulas,[5] Ariel M. Pani,[6] Sabrina L. Spencer,[2] Benjamin L. Martin,[1] and David Q. Matus[1,8,*]

[1]Department of Biochemistry and Cell Biology, Stony Brook University, Stony Brook, NY 11794, USA
[2]Department of Biochemistry and BioFrontiers Institute, University of Colorado Boulder, Boulder, CO 80303, USA.
[3]Department of Biology, Stanford University, Stanford, CA 94305, USA.
[4]Current address: Molecular, Cell and Developmental Biology, University of California Santa Cruz, Santa Cruz, CA 95064, USA
[5]Department of Life Sciences, Imperial College, London SW7 2AZ, UK.
[6]Department of Biology, University of Virginia, Charlottesville, VA 22903, USA.
[7]These authors contributed equally
[8]Lead Contact
*Correspondence: david.matus@stonybrook.edu

SUMMARY

Cell proliferation and terminal differentiation are intimately coordinated during metazoan development. Here, we adapt a cyclin-dependent kinase (CDK) sensor to uncouple these cell cycle-associated events live in *C. elegans* and zebrafish. The CDK sensor consists of a fluorescently tagged CDK substrate that steadily translocates from the nucleus to the cytoplasm in response to increasing CDK activity and consequent sensor phosphorylation. We show that the CDK sensor can distinguish cycling cells in G_1 from terminally differentiated cells in G_0, revealing a commitment point and a cryptic stochasticity in an otherwise invariant *C. elegans* cell lineage. We also derive a predictive model of future proliferation behavior in *C. elegans* and zebrafish based on a snapshot of CDK activity in newly born cells. Thus, we introduce a live-cell imaging tool to facilitate *in vivo* studies of cell cycle control in a wide-range of developmental contexts.

KEYWORDS

cell cycle, proliferation, terminal differentiation, CDK sensor, *C. elegans*, Zebrafish, G_1/G_0

INTRODUCTION

Organismal development requires a delicate balance between cell proliferation and cell cycle arrest. In early embryos, the emphasis is placed on rapid cell proliferation, which is achieved by omitting gap phases (G_1 and G_2) and establishing a biphasic cell cycle that rapidly alternates between DNA synthesis (S phase) and mitosis (M phase) (Edgar and O'Farrell, 1989; Newport and Kirschner, 1982). After several rounds of embryonic cell division, the gap phases are introduced, coincident in many organisms with cell fate decisions and the execution of morphogenetic cell behaviors (Foe, 1989; Grosshans and Wieschaus, 2000). These gap phases are believed to function as commitment points for cell cycle progression decisions. The earliest point of commitment occurs during G_1, which is the focus of this study. Cells either engage in cell cycle progression and enter S phase, or they exit the cell cycle altogether and enter a cell cycle arrested state referred to as G_0 and undergo quiescence or terminal differentiation (Sun and Buttitta, 2017). Although the location of the G_1 commitment point in yeast (Start) and cultured mammalian cells (Restriction Point) has in large part been spatiotemporally mapped and molecularly characterized (Hartwell et al., 1974; Pardee, 1974; Spencer et al., 2013), when metazoan cells make this decision *in vivo* while integrating intrinsic and the extrinsic cues of their local microenvironment during development remains poorly understood. A cell cycle sensor that is amenable to such *in vivo* studies can shed new light on this four-decade-old biological phenomenon.

In 2008, Sakaue-Sawano and colleagues engineered a multicolor fluorescent ubiquitination-based cell cycle indicator (FUCCI) for mammalian cell culture (Sakaue-Sawano et al., 2008). FUCCI has since been adapted for many research organisms (Ozpolat et al., 2017; Zielke and Edgar, 2015). However, FUCCI on its own cannot distinguish between a cell residing in G_1 that will cycle again upon completing mitosis and a cell that is poised to enter G_0 (Oki et al., 2014). Separating G_1 from G_0 is essential to understanding mechanisms controlling cell cycle exit during quiescence or terminal differentiation. To distinguish G_1 from G_0 in mammalian cell culture, Hanh, Spencer and colleagues developed and implemented a single-color ratiometric sensor of cell cycle state comprised of a fragment of human DNA helicase B (DHB) fused to a fluorescent protein that is phosphorylated by CDKs (Hahn et al., 2009; Schwarz et al., 2018; Spencer et al., 2013). Notably, through quantitative measurements of CDK activity, this sensor provided new insights into the proliferation-quiescence decision in cultured mammalian cells by identifying cycling cells that exit mitosis in a CDK-increasing (CDK[inc]) state and quiescent cells that exit

2

80   mitosis in a CDK-low (CDK^{low}) state (Spencer et al., 2013). Nonetheless, a DHB-based CDK
81   sensor has not been utilized to evaluate the proliferation-terminal differentiation decision.
82
83   In this study, we investigate the proliferation-terminal differentiation decision in *C. elegans*
84   and zebrafish, two powerful *in vivo* systems with radically different modes of development. We
85   generate transgenic CDK sensor lines in each organism to examine this decision live at mitotic
86   exit. By quantifying CDK activity, or DHB ratios, at mitotic exit, we are able to predict future cell
87   behavior across several embryonic and post-embryonic lineages. Despite cells generally exiting
88   mitosis with decreased CDK activity levels, we reliably distinguish cycling cells that exit mitosis
89   into G_1, in a CDK^{inc} state, from terminally differentiated cells that exit mitosis into G_0, in a CDK^{low}
90   state. To gain insights into cell cycle progression commitment, we examine the activity of *C.*
91   *elegans cki-1*, a cyclin-dependent kinase inhibitor (CKI) of the Cip/Kip family, demonstrating that
92   endogenous CKI-1 levels are anti-correlated with CDK activity during the proliferation-terminal
93   differentiation decision. We propose that integration of CKI-1 levels in the mother cell and the high
94   CKI-1/low CDK activity at mitotic exit mediate this decision. By utilizing the CDK sensor to predict
95   future cell behavior, we uncover a cryptic stochasticity that occurs in a temperature-dependent
96   fashion in the *C. elegans* vulva, an otherwise invariant and well-characterized lineage. Finally, we
97   reveal cell cycle dynamics in zebrafish, an organism that lacks a defined cell lineage,
98   demonstrating that differentiated embryonic tissues display DHB ratios that correlate with those
99   observed in terminally differentiated G_0 cells in *C. elegans*. Together, we present a tool for
100   visualizing G_1/G_0 dynamics *in vivo* during metazoan development that can be used to study the
101   interplay between cell proliferation and terminal differentiation.
102
103   **RESULTS**
104
105   **Design and Characterization of a Live *C. elegans* CDK Sensor to Define Interphase States**
106   We synthesized a codon-optimized fragment of human DHB comprised of amino acids 994–1087
107   (Hahn et al., 2009; Spencer et al., 2013). The fragment contains four serine sites that are
108   phosphorylated by CDKs in human cells (Moser et al., 2018; Spencer et al., 2013). These serine
109   sites flank a nuclear localization signal (NLS) situated next to a nuclear export signal (NES)
110   (**Figure 1A**). When CDK activity is low, the NLS is dominant over the NES and DHB localizes to
111   the nucleus. However, when CDK activity increases (i.e., during cell cycle entry), the NLS is
112   obstructed and DHB localizes to the cytoplasm (**Figure 1B**). Using this DHB fragment, we
113   generated two CDK sensors by fusing green fluorescent protein (GFP) or two copies of a red
114   fluorescent protein, mKate2 (2xmKate2), to the DHB C-terminus (**Figure 1A**). To visualize the

3

115   nucleus, we co-expressed *his-58*/histone H2B fused to 2xmKate2 or GFP, respectively*,* which is

116   separated from DHB by a P2A self-cleaving viral peptide (Ahier and Jarriault, 2014). We drove

117   the expression of each CDK sensor via a ubiquitous *rps-27* promoter (Ruijtenberg and van den

118   Heuvel, 2015).

119

120   To test both the GFP (**Figure 1C, 1D, S1A**) and 2xmKate2 (**Figure S1B-D)** versions of

121   our CDK sensor, we began by examining cell divisions in the *C. elegans* embryo and germline

122   (**Movie S1**). First, we visualized cells in the embryonic intestine, which is clonally derived from the

123   E blastomere, as these are the first cells in the embryo to have gap phases (Edgar and McGhee,

124   1988). The E blastomere goes through four rounds of divisions to give rise to 16 descendants

125   (E16 cells) about four hours after first cleavage. While 12 of the E16 cells have completed their

126   embryonic divisions at this stage (Leung et al., 1999), four cells called E16* star cells divide once

127   more to generate the 20-celled intestine (E20). Although all E16 cells polarize and show signs of

128   differentiation, the E16* star cells quickly reenter the cell cycle to divide again (Rasmussen et al.,

129   2013; Yang and Feldman, 2015). Thus, we wondered whether our CDK sensor could be used to

130   distinguish between cycling E16* star cells and quiescent E16 cells. To accomplish this, we

131   tracked E16* star cell division from the E16–E20 stage and observed that DHB::GFP localizes in

132   a cell cycle-dependent fashion during these divisions, with DHB::GFP translocating from the

133   nucleus to the cytoplasm and then re-locating to the nucleus at the completion of E16* star cell

134   division (**Figure 1C, S1A**). Consistent with our observations using the GFP version of our CDK

135   sensor in mid-embryogenesis, DHB::2xmKate2 also dynamically translocates from the nucleus to

136   the cytoplasm during cell divisions in the early embryo (**Figure S1B**). Second, we examined the

137   localization of DHB::GFP (**Figure 1D**) and DHB::2xmKate2 (**Figure S1C, S1D**) in the adult *C.*

138   *elegans* germline. Here we detected a gradient of live CDK activity, from high in the distal mitotic

139   progenitor zone to low in the proximal meiotic regions, as described with EdU incorporation and

140   phospho-histone H3 staining (Kocsisova et al., 2018). Together, these results demonstrate that

141   our CDK sensor is dynamic during cell cycle progression in the *C. elegans* embryo and germline.

142

143   The ability to distinguish cycling cells from quiescent cells in the embryo made us wonder

144   whether we could also distinguish cycling cells from terminally differentiated cells post-

145   embryogenesis. Therefore, we examined our CDK sensor in several post-embryonic somatic

146   lineages that undergo proliferation followed by terminal differentiation (Sulston and Horvitz, 1977).

147   Specifically, we selected the sex myoblasts (SM), the somatic sheath (SS) and ventral uterine

148   (VU) cells of the somatic gonad, and the vulval precursor cells (VPCs) (**Figure 1E and E'**). To

149   define each phase of the cell cycle while these lineages are proliferating, we combined static and

150   time-lapse imaging approaches to measure nuclear:cytoplasmic DHB ratios for G_1, S and G_2

151   (**Figure 1F-J, S1E-M**). First, we RNAi depleted the sole *C. elegans* CDK1 homolog, *cdk-1,* to

152   induce a penetrant G_2 phase arrest in the SM cells (**Figure 1F**). Quantification of DHB ratios

153   following *cdk-1* RNAi treatment showed a mean ratio of 1.00±0.28 and 2.36±0.70 in the GFP and

154   2xmKate2 versions of our CDK sensor, respectively (**Figure 1H**). Next, we quantified DHB ratios

155   following time-lapse of SM (**Figure 1F', 1H, S1G**), uterine (**Figure S1E, S1G**) and VPC (**Figure

156   S1F, S1G**) divisions to determine peak values of G_2 CDK activity (**Figure 1I, S1H, S1I**). All

157   lineages exhibited the same CDK sensor localization pattern during peak G_2—that is, maximal

158   nuclear exclusion. Next, for each lineage (**Figure 1F'', S1E', S1F'**), we quantified DHB ratios 20

159   minutes after anaphase from our time-lapses to determine a threshold for G1 phase CDK activity.

160   In G1, DHB::GFP and DHB::2xmKate2 were nuclear localized after mitotic exit with mean ratios

161   of 0.59±0.11 and 0.97±0.20 in SMs, 0.67±0.10 and 1.13±0.17 in uterine cells, and 0.35±0.14 and

162   0.58±0.32 in VPCs (**Figure 1H, 1I, S1G-I**). Finally, we paired DHB::2xmKate2 with a reporter for

163   S phase, fusing GFP to the sole *C. elegans* proliferating cell nuclear antigen (PCNA)

164   homolog, *pcn-1*, expressed under its own endogenous promoter at single copy. Although nuclear

165   localized throughout the cell cycle, PCNA forms sub-nuclear puncta solely in S (Brauchle et al.,

166   2003; Dwivedi et al., 2019; Strzyz et al., 2015; Zerjatke et al., 2017). Analysis of time-lapse data

167   found that punctate expression of PCN-1::GFP correlated with mean DHB::2xmKate2 ratios of

168   0.89±0.16 in SM (**Figure 1G, 1J, Movie S2**), 1.00±0.10 in uterine (**Figure S1J, S1K**) and

169   1.02±0.22 in VPC (**Figure S1J, S1K**) lineages. Despite individual lineages showing differences

170   in CDK activity (**Figure S1G**), primarily in G_1, we can establish DHB ratios for each interphase

171   state (G_1/S/G_2) across several post-embryonic somatic lineages using either CDK sensor and

172   recommend pairing with a PCNA reporter for precise determination of interphase state

173   boundaries. We next wondered if we could distinguish G_1 from G_0 as these somatic lineages exit

174   their final cell division; therefore, allowing us to visibly and quantitatively detect terminal

175   differentiation *in vivo*. We mainly chose the DHB::GFP version of our CDK sensor to conduct the

176   following experiments as it was more photostable.

177

178   **CDK^low Activity after Mitotic Exit is Predictive of Terminal Differentiation**

179   In asynchronously dividing MCF10A epithelial cell lines, cells that exited mitosis into a CDK2^low

180   state had a high probability of staying in G_0 compared to cells that exited at a CDK2^inc state

181   (Spencer et al., 2013). We therefore wanted to determine whether the cytoplasmic:nuclear ratio

182   of DHB::GFP following an *in vivo* cell division could be used to predict if a cell will enter G_1 and

183   divide again or enter G_0 and terminally differentiate. Taking advantage of the predictable cell

5

184   lineage pattern of *C. elegans*, we quantitatively correlated DHB::GFP ratios with the decision to

185   proliferate or terminally differentiate. We first quantified DHB::GFP ratios from time-lapse

186   acquisitions of SM cell divisions. The SM cells undergo three rounds of cell division during the L3

187   and L4 larval stages before terminally differentiating into uterine and vulval muscle (**Figure 2A**)

188   (Sulston and Horvitz, 1977). Quantification of DHB::GFP in this lineage revealed that shortly after

189   the first and second divisions, CDK activity increases immediately after mitotic exit from an

190   intermediate level, which we designate as a CDK^{inc} state (**Figure 2B, 2C, Movie S3**), Conversely,

191   CDK activity following the third and terminal division remains low, designated as a CDK^{low} state.

192   Bootstrap analyses support a significant difference in DHB::GFP ratios between pre-terminal

193   (CDK^{inc}) and terminal divisions, but not among pre-terminal divisions (**Figure S2A-C**). We then

194   quantified DHB::GFP ratios during the division of two somatic gonad lineages, the VU and SS

195   cells. They both undergo several rounds of division during the L3 larval stage and terminally

196   differentiate in the early L4 stage (**Figure 2D**) (Sulston and Horvitz, 1977). We quantified a pre-

197   terminal division and the subsequent division that leads to terminal differentiation. Similar to the

198   SM lineage, both somatic gonad lineages exit the round of cell division prior to their final division

199   into a CDK^{inc} state and then exit into a CDK^{low} state following their terminal differentiation (**Figure**

200   **2E, 2F, S2D-F, Movie S4**). Bootstrap analyses support a significant difference between

201   DHB::GFP ratios in pre-terminal versus terminal divisions in the developing somatic gonad

202   (**Figure S2D**).

203

204   Next, we sought to determine how the CDK sensor behaves under conditions in which

205   cells are experimentally forced into G_0. To accomplish this, we generated a single copy transgenic

206   line of mTagBFP2-tagged CKI-1, the *C. elegans* homolog of p21^{Cip1}/p27^{Kip1}, under an inducible

207   heat shock promoter (*hsp*), paired with a *rps-0*>DHB::mKate2 variant of the CDK sensor. Induced

208   expression of CKI-1 is expected to result in G_0 arrest (Hong et al., 1998; Matus et al., 2014; van

209   der Horst et al., 2019). Indeed, in the SM and uterine lineages, induced expression of CKI-1

210   resulted in cells entering a CDK^{low} G_0 state, with mean DHB ratios of 0.10±0.05 and 0.12±0.05,

211   respectively (**Figure 2G**) as compared to control animals that lacked heat shock-induced

212   expression (SM: 0.99±0.82, uterine: 0.71±0.35) or lacked the inducible transgene (SM:

213   0.96±0.77, uterine: 1.00±0.37). Thus, induced G_0 arrest by ectopic expression of CKI-1 is

214   functionally equivalent, by CDK activity levels, to the G_0 arrest that occurs following mitotic exit in

215   an unperturbed cell destined to undergo terminal differentiation.

216

217   We next examined the divisions of the 1°- and 2°-fated VPC lineage. The *C. elegans* vulva

218   is derived from three cells (P5.p–P7.p), which undergo three rounds of cell division during the L3

219   and early L4 larval stages (**Figure 3A, 3B**) (Katz et al., 1995; Sternberg and Horvitz, 1986; Sulston
220   and Horvitz, 1977). Rather than giving rise to 24 cells, the two D cells, the innermost
221   granddaughters of the 2°-fated P5.p and P7.p, terminally differentiate one round of cell division
222   early. This results in a total of 22 cells which comprise the adult vulva (Katz et al., 1995; Sulston
223   and Horvitz, 1977). Quantification of DHB::GFP ratios during VPC divisions yielded the expected
224   pattern. The daughters of P5.p–P7.p all exited their first division into a CDK^{inc} state (**Figure 3C,**
225   **3D).** After the next division, the 12 granddaughters of P5.p–P7.p (named A–F symmetrically) are
226   born, including the terminally differentiated D cell (Katz et al., 1995; Sulston and Horvitz, 1977).
227   At this division, the strong nuclear localization of DHB::GFP in the D cell was in stark contrast to
228   the remaining proliferating VPCs. The D cell exited into and remained in a CDK^{low} state, while the
229   remaining VPCs exited into a CDK^{inc} state and continued to progress through the cell cycle
230   (**Figure 3C, 3D, Movie S5**). All remaining VPCs exited into a CDK^{low} state at their terminal
231   division. Consistent with these results, bootstrap analyses (**Figure S2G-M**) support our qualitative
232   results, such that we can quantitatively distinguish between a cell that has completed mitosis and
233   will continue to cycle (CDK^{inc}) from a cell that exits mitosis and enters a terminally differentiated
234   G_0 state (CDK^{low}).
235
236   **CKI-1 Levels Peak Prior to Terminal Differentiation**
237   In mammalian cell culture, endogenous levels of $p21^{Cip1}$ during G_2 are predictive of whether a cell
238   will go on to divide or enter quiescence/senescence/terminal differentiation (Hsu et al., 2019;
239   Moser et al., 2018; Overton et al., 2014; Spencer et al., 2013). This raises the intriguing possibility
240   that endogenous levels of CKI-1 in *C. elegans* correlate with CDK^{low} or CDK^{inc} activity. To co-
241   visualize CKI-1 dynamics with our CDK sensor, we inserted a N-terminal GFP tag into the
242   endogenous locus of *cki-1* via CRISPR/Cas9 and introduced a DHB::2xmKate2 variant of the
243   sensor (devoid of histone H2B) into this genetic background. Since endogenous levels of
244   GFP::CKI-1 were too dim for time-lapse microscopy, likely due to its short half-life (Yang et al.,
245   2017), we collected a developmental time series of static images over the L3 and L4 larval stages
246   to characterize GFP::CKI-1 levels during pre-terminal and terminal divisions in the VPC lineage.
247   We detected generally low levels of GFP::CKI-1 at the Pn.p 2-cell stage (**Figure 4A, 4B, S3A-C**).
248   In their daughter cells, at the Pn.p 4-cell stage, we detected an increase in GFP::CKI-1 levels in
249   cycling cells prior to their next cell division, peaking in G_2 (**Figure 4A, 4C, S3A-C**). Notably, the D
250   cell, which becomes post-mitotic after this cell division, exits mitosis with higher levels of
251   GFP::CKI-1 than its CD mother (**Figure 4A and S3B**). This trend holds true for the remaining
252   VPCs during terminal differentiation at the Pn.p 6-cell and 8-cell stage, which show high levels of

7

253   GFP::CKI-1 that peak immediately after mitotic exit and remain high during the post-mitotic L4

254   stage (**Figure 4A, 4D, 4E, S4A-C**). We also observed increasing levels of GFP::CKI-1 in the G_2

255   phase of mother cells that peak in their terminal daughter cells in the uterine (**Figure S3D**) and

256   SM cell lineages (**Figure S3E**). Thus, levels of GFP::CKI-1 increase in mother cells prior to

257   terminal differentiation and remain high upon mitotic exit in daughter cells with CDK^{low} activity.

258   These results elucidate a proliferation-terminal differentiation decision process that is already

259   underway in G_2 of the previous cell cycle and is in part controlled by CKI-1 in the mother cell.

260

261   During our collection of static images of GFP::CKI-1 animals, we observed significant

262   deviations in the expected VPC lineage pattern in the early L4 larval stage. In particular, we noted

263   that many cells appeared to bypass their final division and undergo early terminal differentiation

264   with coincident high levels of GFP::CKI-1 and low DHB ratios. We hypothesized that the line we

265   generated could be behaving as a gain-of-function mutant, as GFP insertions at the N-terminus

266   could interfere with proteasome-mediated protein degradation of CKI-1 (Bloom et al., 2003). The

267   penetrance of this early terminal differentiation defect varied across VPC lineages. While the A

268   (2% of cases observed) and E (3% of cases observed) lineages showed a low penetrance of this

269   early terminal differentiation defect, the B (26% of cases observed) and F (58% of cases

270   observed) lineages showed a moderate penetrance (**Figure 4F, 4G**). We speculate that the A

271   and E lineages are largely insensitive to the gain-of-function mutant because CKI-2, an

272   understudied paralog of CKI-1, is the dominant CKI in these cells. The C cell, sister to the

273   terminally differentiated D cell, had a highly penetrant early terminal differentiation defect (98% of

274   cases observed; **Figure 4F, 4G**). Consistent with our finding that high levels of endogenous

275   GFP::CKI-1 can lead to early terminal differentiation, heat shock-induced CKI-1 expression

276   uniformly drove VPCs into a CDK^{low} G_0 state with mean DHB ratios of 0.11±0.05 (**Figure 4H**) as

277   compared to control animals that lacked heat shock-induced expression (0.46±0.87) or lacked the

278   inducible *cki-1* transgene (0.47±0.42). Together, these results demonstrate that cycling cells are

279   highly sensitive to levels of CKIs and that increased expression can induce a terminally

280   differentiated G_0 state.

281

282   **CDK Activity Predicts a Cryptic Stochastic Fate Decision in an Invariant Cell Lineage**

283   A strength of *C. elegans* is the organism's robust ability to buffer external and internal

284   perturbations to maintain its invariant cell lineage. However, not all cell divisions that give rise to

285   the 959 somatic cells are completely invariant. Studies have identified several lineages, including

286   the vulva, in *C. elegans* where environmental stressors, genetic mutations and/or genetic

287   divergence of wild isolates leads to stochastic changes in a highly invariant cell fate pattern

288   (Braendle and Felix, 2008; Hintze et al., 2020; Katsanos et al., 2017). Thus, we wondered if the

289   CDK sensor generated here could be utilized to visualize and predict stochastic lineage decisions

290   during *C. elegans* development.

291

292   The VPC lineage that gives rise to the adult vulva is invariant (**Figure 5A, S4A**) (Sulston

293   and Horvitz, 1977). However, at high temperatures it has been observed that the D cell, the inner-

294   most granddaughter of P5.p or P7.p, will go on to divide (**Figure 5A**) (Sternberg, 1984; Sternberg

295   and Horvitz, 1986). Unexpectedly, we noticed a rare occurrence of D cells expressing elevated

296   DHB ratios during the course of time-lapse analysis of VPC divisions captured under standard

297   laboratory conditions. To determine the penetrance of the cycling D cell phenotype, we inspected

298   each of our CDK sensor lines grown at 25°C, a high temperature that is still within normal range

299   for *C. elegans*. In both strains we observed a cycling D cell with a 2-10% penetrance (**Figure 5B,**

300   **S4B**). To test whether this cycling D cell phenotype resulted from the presence of the DHB

301   transgene or environmental stressors, such as temperature fluctuation, we examined the VPC

302   lineage in animals lacking the CDK sensor at 25°C and 28°C. At 25°C, we observed a low

303   penetrance (2%) of cycling D cells in a strain expressing an endogenously tagged DNA licensing

304   factor, CDT-1::GFP (**Figure 5B, S4B**), which is cytosolic in cycling cells (Matus et al., 2014;

305   Matus et al., 2015). From lineage analysis, L2 larvae, expressing a seam cell reporter (*scm*>GFP),

306   that were temperature shifted from 20°C to 28°C displayed approximately a 30% occurrence of

307   extra D cell divisions (**Figure S4C-E**). Lastly, we wanted to determine whether D cells that show

308   CDK^{inc} activity divide. To accomplish this, we collected time-lapses of DHB::GFP animals grown

309   at 25°C. These time-lapses revealed 10 occurrences of D cells born into a CDK^{inc} rather than a

310   CDK^{low} (**Figure 5C, 5D, Movie S6**). In all 10 cases, the CDK^{inc} D cell goes on to divide (**Figure**

311   **S4A**). Thus, we find that CDK activity shortly after mitosis is a strong predictor of future cell

312   behavior, even in rare stochastic cases of extra cell divisions in *C. elegans*, an organism with a

313   well-defined cell lineage.

314

315   **Generation of Inducible CDK Sensor Transgenic Lines in Zebrafish**

316   To investigate the predictive capability of DHB ratios in zebrafish, we generated two CDK sensor

317   lines with different fluorescent protein combinations, DHB-mNeonGreen (mNG) and DHB-

318   mScarlet (DHB-mSc) with H2B-mSc and H2B-miRFP670, respectively, to allow for flexibility with

319   imaging and experimental design (**Figure 6A**). Both transgenes are under the control of the

320   *hsp70l* heat shock-inducible promoter, which produces robust ubiquitous expression after shifting

321   the temperature from 28.5°C to 40°C for 30 minutes (Halloran et al., 2000; Shoji et al., 1998). We

322   also generated a transgenic line, *Tg(ubb:Lck-mNG)*, that ubiquitously labels the plasma

9

323   membrane with mNG, which we crossed into the HS:DHB-mSc-2A-H2B-miRFP670 line to
324   simultaneously visualize CDK activity (DHB-mSc), segment nuclei (H2B-miRFP670) and segment
325   the plasma membrane (LCK-mNG) (**Figure 6A**).

327   To verify that both CDK sensor lines localize DHB in a cell cycle-dependent manner, we
328   first used time-lapse microscopy and quantified DHB ratios across cell divisions in the tailbud of
329   bud or 22 somite-stage embryos to determine peak G_2 and G_1 DHB ratios (**Figure 6B-D**). We
330   observed the expected localization pattern for both CDK sensor lines, with maximal nuclear
331   exclusion of the sensor shortly before mitosis in G2 (3.42±0.56 and 6.57±2.00) and low DHB
332   ratios (0.69±0.17 (mNG) and 0.51±0.21 (mSC)) representing nuclear accumulation of the sensor
333   shortly after mitosis in G1 (**Figure 6C, 6D**). Thus, we conclude that both CDK sensor lines localize
334   in a cell cycle-dependent fashion, and that quantitative measurements can be used to determine
335   interphase states.

337   Next, using both DHB transgenic lines, we examined CDK activity in a number of defined
338   embryonic tissues. Imaging of the developing tailbud reveled cells in all phases of the cell cycle
339   with a mean DHB ratios of 1.95±1.74 (mNG) and 1.67±2.05 (mSC) (**Figure 6E, 6F**). The tailbud
340   of vertebrate embryos contain neuromesodermal progenitors (NMPs) (Martin, 2016), which in
341   zebrafish have been reported to be predominantly arrested in the G_2 phase of the cell cycle
342   (Bouldin et al., 2014). Consistent with this, we observed cells with high CDK activity in the tailbud
343   (**Figure 6E, S5A** orange arrows). This enrichment is eliminated when embryos are treated with
344   the CDK4/6 inhibitor palbociclib, leading to a significant increase of cells in the tailbud with low
345   CDK activity (0.58±0.31), similar in range to the G_1/G_0 values we measured during time-lapse
346   (0.69±0.17) (**Figure S5D-F**). Finally, we made the surprising observation that primitive red blood
347   cells in the intermediate cell mass of 24 hours post-fertilization (hpf) embryos, which are nucleated
348   in zebrafish, display high CDK activity (3.00±0.97) indicating that they are exclusively in the G_2
349   phase of the cell cycle (**Figure S5B**), suggesting that cell cycle regulation may be important for
350   hematopoiesis (Bronnimann et al., 2018; De La Garza et al., 2019)

352   **Visualization of Proliferation and Terminal Differentiation during Zebrafish Development**
353   To examine differences between proliferating and terminally differentiated cells, we examined
354   CDK activity in the somites, which are segmental mesodermal structures that give rise to
355   terminally differentiated skeletal muscle cells and other cell types (Martin, 2016). In the most
356   recently formed somites at 24 hpf, cells can be observed in all phases of the cell cycle (**Figure
357   6G, 6H**). Consistent with what we observed in the NMPs in the tailbud, treatment with palbociclib

358   also caused somite cells to arrest with low CDK activity (0.33±0.42) in G_1/G_0 (**Figure S5D-F**).

359   Recently formed somites contain a subpopulation of cells called adaxial cells, which are

360   positioned at the medial edge of the somite next to the axial mesoderm. These are the slow

361   muscle precursors and are considered to be in a terminally differentiated state through the

362   cooperative action of Cdkn1ca (p57) and Myod (Osborn et al., 2011). As opposed to the majority

363   of cells in the lateral regions of recently formed somites, adaxial cells possess low CDK activity

364   (0.13±0.04 (mNG)) (**Figure S5C**). At later stages, the majority of cells in the lateral regions of the

365   somite will differentiate into fast skeletal muscles fibers, which are also considered to be in a

366   terminally differentiated state (Halevy et al., 1995). Examination of DHB ratios at 72 hpf skeletal

367   muscle fibers revealed they have low CDK activity (0.14±0.04 (mNG) and 0.13±0.04 (mSc)),

368   similar to the adaxial cells, but significantly different than the mean DHB ratios of undifferentiated

369   cells at 24 hours (0.82±0.70 (mNG) and 0.99±0.084 (mSc)) (**Figure 6A, 6C**). Thus, from our static

370   imaging, we can identify cell types with low CDK activity that are thought to be terminally

371   differentiated.

372

373   We next sought to determine if we can differentiate between the G_1 and G_0 state based

374   on ratiometric quantification of DHB. We compared the terminally differentiated muscle and

375   epidermal cells to notochord progenitor cells, which are held transiently in G_1/G_0 before re-

376   entering the cell cycle upon joining the notochord (Sugiyama et al., 2014; Sugiyama et al., 2009)

377   (**Figure 6I**). Notably, the mean DHB-mNG ratio of the notochord progenitors (0.32±0.08) is

378   significantly higher than the DHB-mNG ratio of the differentiated epidermis (0.13±0.03) (**Figure**

379   **6J**). This value is consistent in notochord progenitors at two other earlier developmental stages,

380   90% epiboly (0.28±0.08) and 18 somites (0.27±0.09) (**Figure 6J**). The DHB-mSc ratio in the

381   notochord progenitors (0.33±0.08) is also significantly different than the differentiated epidermis

382   (0.09±0.04) (**Figure 6J**). Based on this difference in DHB ratios between notochord progenitors

383   and terminally differentiated cell types, including muscle (**Figure 6H**) and epidermis (**Figure 6J**),

384   and our knowledge of the normal biology of these cells, we conclude that the CDK sensor can

385   distinguish between a cycling G_1 state and a terminally differentiated G_0 state in the zebrafish.

386

387   **A Bifurcation in CDK Activity at Mitosis is Conserved in *C. elegans* and Zebrafish**

388   We next investigated whether zebrafish cells separate into G_1/CDK^{inc} and G_0/CDK^{low} populations

389   as they do in the nematode *C. elegans* and whether these CDK activity states are a general

390   predictor of future cell behavior in both animals. First, we plotted all of the time-lapse CDK sensor

391   data we collected in *C. elegans* (**Figure 7A, 7B**) and zebrafish (**Figure 7C, 7D**). For *C. elegans*,

392   plotting of all CDK sensor trace data, irrespective of lineage, demonstrated that cells entering a

393 CDK^{low} state after mitosis corresponded to terminally differentiated cells, while cells that exited

394 mitosis into a CDK^{inc} state corresponded to cells from pre-terminal divisions. For zebrafish, in a

395 lineage agnostic manner, we plotted all the traces from the tailbud and found that these data could

396 also be classified into CDK^{low} and CDK^{inc} populations.

397

398 As we were able to detect a rare stochastic lineage change in the *C. elegans* vulval lineage

399 (**Figure 5**), we selected all CDK sensor trace data from the *C. elegans* VPCs (**Figure S6A**) and

400 used this data to build a classifier to predict pre-terminal (G_1) vs terminal (G_0) cell fates based on

401 CDK activity after anaphase (**Figure S6A-C**). Cross-examining our modeling with the known cell

402 VPC lineage demonstrated that at 20 minutes after anaphase we had 85% accuracy in predictions

403 with near perfect prediction 60 minutes after anaphase (**Figure S6B**). To test the predictive power

404 of the classifier, we analyzed CDK trace data from the births of C and D cells, where some D cells

405 stochastically divide (**Figure 5**). Our classifier correctly predicted cell fate 92% of the time (**Figure**

406 **S6**). Together, these results demonstrate that during development, cycling cells encounter a

407 bifurcation in CDK activity following mitosis where they either: (1) increase in CDK activity and

408 become poised to cycle, or (2) exit into a a CDK^{low} state and undergo terminal differentiation

409 (**Figure 7E**). Thus, we suggest a model where cells from developing tissue in *C. elegans* and

410 zebrafish must cross an early commitment point in the cell cycle where these cells must make the

411 decision to divide or terminally differentiate. The decision to undergo terminal differentiation is

412 crucial to tissue integration and organization and is controlled by the activity of evolutionarily

413 conserved CKI(s) in the mother cell (**Figure 7E**) that control daughter cell CDK activity.

414
415 **DISCUSSION**
416
417 **A CDK Sensor for Live-Cell In Vivo Imaging of Interphase States and the G_1/G_0 Transition**

418 We introduce here a CDK activity sensor to visually monitor interphase and the proliferation-

419 terminal differentiation decision in real-time and *in vivo* in two widely used research organisms,

420 *C. elegans* and zebrafish. This sensor, which reads out the phosphorylation of a DHB peptide by

421 CDKs (Hahn et al., 2009; Spencer et al., 2013), allows for quantitative assessment of cell cycle

422 state, including G_0. The use of FUCCI in zebrafish (Bouldin and Kimelman, 2014; Sugiyama et

423 al., 2009) and past iterations of a CDK sensor in *C. elegans* (Deng et al., 2020; Dwivedi et al.,

424 2019; van Rijnberk et al., 2017) and *Drosophila* (Hur et al., 2020) have been informative in

425 improving our understanding of cell cycle regulation of development, but have not addressed the

426 proliferation-terminal differentiation decision. The DHB transgenic lines generated in this study

427 will allow researchers to distinguish G_1 from G_0 shortly after a cell has divided and directly study

428   G_0-related cell behaviors, such as terminal differentiation, quiescence and senescence, in living

429   organisms.

430

431   CDK sensors have been used previously to visualize the difference between proliferative

432   and quiescent cells in asynchronous mammalian cell culture populations (Arora et al., 2017;

433   Cappell et al., 2016; Gast et al., 2018; Gookin et al., 2017; Miller et al., 2018; Moser et al., 2018;

434   Overton et al., 2014; Spencer et al., 2013; Yang et al., 2015). As mammalian cells complete

435   mitosis, they are born into either a CDK2[inc] state where they are more likely to divide again, or a

436   CDK2^{low} state where they remain quiescent for longer periods of time. Here we have examined

437   the CDK activity state of cells in an invertebrate with a well-defined and invariant lineage, *C.

438   elegans*, and a vertebrate that lacks a defined cell lineage, the zebrafish. In both contexts, we can

439   visually and quantitatively differentiate between cells that are in a CDK[inc] state following cell

440   division and cells that are in a CDK[low] state. Strikingly, in *C. elegans* these states precisely

441   correlate with the lineage pattern of the three post-embryonic tissues we examined: the SM cells,

442   uterine cells and VPCs. Cells born into a CDK[inc] state represented pre-terminal divisions, whereas

443   cells born into a CDK[low] state were terminally differentiated. By distinguishing these two states in

444   CDK activity, we were able to accurately identify shortly after cell birth a rare stochasticity that

445   was first described through careful end-point lineage analysis nearly 36 years ago in the *C.

446   elegans* vulval lineage (Sternberg, 1984; Sternberg and Horvitz, 1986). Further, statistical

447   modeling demonstrated that we could predict future cell behavior with >85% accuracy in *C.

448   elegans* just 20 minutes after anaphase and accurately categorized the few cases of stochastic

449   extra cell division we captured during our time-lapse recordings. In zebrafish, we found that we

450   could readily distinguish between CDK[inc] cells in G_1, such as notochord progenitors which re-enter

451   the cell cycle after joining the notochord, and tissues that are terminally differentiated and contain

452   CDK^{low} cells in G_0, such as skeletal muscle and epidermis. Thus, in both organisms the CDK

453   sensor can be easily used to separate G_1 from G_0 without the need for multiple fluorescent

454   reporters (Bajar et al., 2016; Oki et al., 2014) or fixation and antibody staining for FACS analysis

455   (Tomura et al., 2013).

456

457   **In Vivo Evidence of a G_2 Commitment Point in the Metazoan Cell Cycle**

458   The classic model of the Restriction Point, the point in G_1 at which cells in culture decide to commit

459   to the cell cycle and no longer require growth factors (e.g., mitogens), is that mammalian cells are

460   born uncommitted and that the cell cycle progression decision is not made until several hours

461   after mitosis (Jones and Kazlauskas, 2001; Pardee, 1974; Zetterberg and Larsson, 1985; Zwang

462   et al., 2011). An alternative model has been proposed in studies using single-cell measurements

13

463   of CDK2 activity in asynchronous populations of MCF10A cells (Spencer et al., 2013) and other

464   nontumorigenic as well as tumorigenic cell lines (Moser et al., 2018). This model extends the

465   classic Restriction Point model for cell cycle commitment. During the G_2 phase of the cell cycle,

466   the mother cell is influenced by levels of p21 and cyclin D and these levels affect the

467   phosphorylation state of Rb in CDK^{low} and CDK^{inc} daughter cells, respectively (Min et al., 2020;

468   Moser et al., 2018). In CDK^{low} daughter cells, phospho-Rb is low and these cells are still sensitive

469   to mitogens. Whether cells *in vivo* coordinate cell cycle commitment with levels of CKI and CDK

470   over this extended Restriction Point is poorly understood.

471

472   By first quantifying the cytoplasmic:nuclear ratio of the CDK sensor in time-lapse

473   recordings of cell divisions in *C. elegans* somatic lineages, we were able to use DHB ratios as a

474   proxy for CDK levels to distinguish two populations of daughter cells: the first being actively cycling

475   cells in a CDK^{inc} state (G_1), and the second being terminally differentiated cells in a CDK^{low} state

476   (G_0). We then quantified cytoplasmic:nuclear ratio of the CDK sensor in time-lapse recordings of

477   cell divisions in zebrafish and were also able to distinguish two populations of daughter cells. As

478   data from asynchronous cell culture studies suggest that the decision to commit to the cell cycle

479   is made by the mother cell as early as G_2 (Moser et al., 2018; Spencer et al., 2013), we wanted

480   to determine if this same phenomenon occurred *in vivo*. To accomplish this, we endogenously

481   tagged one of two CKIs in the *C. elegans* genome, *cki-1*, with GFP using CRISPR/Cas9. We

482   paired static live-cell imaging of GFP::CKI-1 with DHB::2xmKate2 during vulval development.

483   Similar to *in vitro* experiments (Moser et al., 2018; Spencer et al., 2013), we found that mother

484   cells whose daughters are born into a CDK^{inc} G_1 state will divide again, expressing low levels of

485   GFP::CKI-1. In contrast, mother cells of daughters that will differentiate express a peak of

486   GFP::CKI-1 in G_2 which increases as daughter cells are born into a CDK^{low} G_0 state. Thus, our

487   data demonstrate that an extended Restriction Point exists in the cell cycle of intact Metazoa, and

488   that the *in vivo* proliferation-terminal differentiation decision can be predicted in *C. elegans* by

489   CKI/CDK activity shortly after mitotic exit.

490

491   **Conclusion**

492   We demonstrate here that the CDK sensor functions in both *C. elegans* and zebrafish to read out

493   cell cycle state dynamically, and unlike other cell cycle sensors, can distinguish between

494   proliferative and terminally differentiated cells within an hour of cell birth. As nematodes and

495   vertebrates last shared a common ancestor over 500 million years ago, this suggests that the

496   CDK sensor is likely to function in a similar fashion across Metazoa. Thus, this broad functionality

497   will provide a powerful tool to examine fundamental questions such as the relationship between

498 cell cycle state and cell fate during normal development, cellular reprogramming and tissue

499 regeneration. Finally, as an increasing body of evidence suggests that cell cycle state impinges

500 on morphogenetic events ranging from gastrulation (Grosshans and Wieschaus, 2000; Murakami

501 et al., 2004), convergent extension (Leise and Mueller, 2004) and cellular invasion (Kohrman and

502 Matus, 2017; Matus et al., 2015; Medwig-Kinney et al., 2020), this CDK sensor will provide the

503 means to increase our understanding of the relationship between interphase states and

504 morphogenesis during normal development and diseases arising from cell cycle defects, such as

505 cancer.

SUPPLEMENTAL INFORMATION

509 Supplemental Information includes Extended Experimental Procedures, six figures, one table,
510 and seven movies, which can be found online with this article.

ACKNOWLEDGEMENTS

AUTHOR CONTRIBUTIONS

534 Conceptualization, R.C.A., A.Q.K., M.A.Q.M., M.D.S., J.L.F., S.L.S., B.L.M. and D.Q.M.;
535 Methodology, R.C.A., A.Q.K., M.A.Q.M., N.J.P., J.J.S., T.N.M-K., S.L., R.D.M., W.Z., B.L.M., and
536 D.Q.M.; Formal Analysis, R.C.A., M.A.Q.M., N.J.P., A.Q.K., T.N.M-K., M.M., S.L.S, B.L.M. and
537 D.Q.M.; Investigation, R.C.A., A.Q.K., M.A.Q.M., N.J.P., J.J.S., M.D.S., O.B.A., N.K., N.W., M.B.,
538 A.M.P., B.L.M. and D.Q.M.; Writing, M.A.Q.M, R.C.A., A.Q.K., T.N.M-K., B.L.M and D.Q.M.;
539 Visualization, R.C.A., M.A.Q.M, T.N.M-K. and D.Q.M.; Funding Acquisition, A.Q.K., R.C.A.,
540 N.J.P., T.N.M-K., B.L.M. and D.Q.M.

DECLARATION OF INTERESTS

544 The authors declare no competing interests.

EXPERIMENTAL PROCEDURES

C. elegans **Strains**

C. elegans strains were cultured in standard conditions at 15-25°C on NGM plates with *E. coli* OP50. In the text and figures, we designate linkage to a promoter with a greater than symbol (>) and use a double colon (::) for linkages that fuse open reading frames (Ziel et al., 2009). See **Extended Experimental Procedures** and the **Key Resources Table** for details about alleles and transgenes generated in this study.

Zebrafish Lines

All zebrafish experiments and husbandry were performed with approval from the Stony Brook University Institutional Animal Care and Use Committee. See **Extended Experimental Procedures** and the **Key Resources Table** for details about the transgenic lines generated used in this study.

RNAi, Heat Shock Induction and Chemical Inhibitors

RNAi was delivered by feeding worms *E. coli* HT115(DE3) expressing double-stranded RNA (dsRNA) targeted against *control* (L4440) and *cdk-1*. Expression of *cki-1* was induced using a ubiquitous heat shock promoter. The inhibitor used in zebrafish was PD-0332991, a CDK4/6 inhibitor. See **Extended Experimental Procedures**.

Live-Cell Microscopy

For microscopes and imaging conditions, see **Extended Experimental Procedures**.

Image Processing and Statistical Analyses

Image processing was performed in Fiji and statistical analyses were performed in MATLAB. See **Extended Experimental Procedures**.

**REFERENCES**

1.   Ahier, A., and Jarriault, S. (2014). Simultaneous expression of multiple proteins under a single promoter in Caenorhabditis elegans via a versatile 2A-based toolkit. Genetics *196*, 605-613.

2.   Arora, M., Moser, J., Phadke, H., Basha, A.A., and Spencer, S.L. (2017). Endogenous Replication Stress in Mother Cells Leads to Quiescence of Daughter Cells. Cell Rep *19*, 1351-1364.

3.   Bajar, B.T., Lam, A.J., Badiee, R.K., Oh, Y.H., Chu, J., Zhou, X.X., Kim, N., Kim, B.B., Chung, M., Yablonovitch, A.L.*, et al.* (2016). Fluorescent indicators for simultaneous reporting of all four cell cycle phases. Nat Methods *13*, 993-996.

4.   Bloom, J., Amador, V., Bartolini, F., DeMartino, G., and Pagano, M. (2003). Proteasome-mediated degradation of p21 via N-terminal ubiquitinylation. Cell *115*, 71-82.

5.   Bouldin, C.M., and Kimelman, D. (2014). Dual fucci: a new transgenic line for studying the cell cycle from embryos to adults. Zebrafish *11*, 182-183.

6.   Bouldin, C.M., Snelson, C.D., Farr, G.H., 3rd, and Kimelman, D. (2014). Restricted expression of cdc25a in the tailbud is essential for formation of the zebrafish posterior body. Genes Dev *28*, 384-395.

7.   Braendle, C., and Felix, M.A. (2008). Plasticity and errors of a robust developmental system in different environments. Dev Cell *15*, 714-724.

8.   Brauchle, M., Baumer, K., and Gonczy, P. (2003). Differential activation of the DNA replication checkpoint contributes to asynchrony of cell division in C. elegans embryos. Curr Biol *13*, 819-827.

9.   Bronnimann, D., Annese, T., Gorr, T.A., and Djonov, V. (2018). Splitting of circulating red blood cells as an in vivo mechanism of erythrocyte maturation in developing zebrafish, chick and mouse embryos. J Exp Biol *221*.

10.   Cappell, S.D., Chung, M., Jaimovich, A., Spencer, S.L., and Meyer, T. (2016). Irreversible APC(Cdh1) Inactivation Underlies the Point of No Return for Cell-Cycle Entry. Cell *166*, 167-180.

11.   De La Garza, A., Cameron, R.C., Gupta, V., Fraint, E., Nik, S., and Bowman, T.V. (2019). The splicing factor Sf3b1 regulates erythroid maturation and proliferation via TGFbeta signaling in zebrafish. Blood Adv *3*, 2093-2104.

12.   Deng, T., Stempor, P., Appert, A., Daube, M., Ahringer, J., Hajnal, A., and Lattmann, E. (2020). The Caenorhabditis elegans homolog of the Evi1 proto-oncogene, egl-43, coordinates G1 cell cycle arrest with pro-invasive gene expression during anchor cell invasion. PLoS Genet *16*, e1008470.

13.   Dwivedi, V.K., Pardo-Pastor, C., Droste, R., Denning, D.P., Rosenblatt, J., and Horvitz, H.R. (2019). Cell cycle S-phase arrest drives cell extrusion. bioRxiv, 839845.

14.   Edgar, B.A., and O'Farrell, P.H. (1989). Genetic control of cell division patterns in the Drosophila embryo. Cell *57*, 177-187.

15.   Edgar, L.G., and McGhee, J.D. (1988). DNA synthesis and the control of embryonic gene expression in C. elegans. Cell *53*, 589-599.

16.   Foe, V.E. (1989). Mitotic domains reveal early commitment of cells in Drosophila embryos. Development *107*, 1-22.

17.   Gast, C.E., Silk, A.D., Zarour, L., Riegler, L., Burkhart, J.G., Gustafson, K.T., Parappilly, M.S., Roh-Johnson, M., Goodman, J.R., Olson, B.*, et al.* (2018). Cell fusion potentiates tumor heterogeneity and reveals circulating hybrid cells that correlate with stage and survival. Sci Adv *4*, eaat7828.

18.   Gookin, S., Min, M., Phadke, H., Chung, M., Moser, J., Miller, I., Carter, D., and Spencer, S.L. (2017). A map of protein dynamics during cell-cycle progression and cell-cycle exit. PLoS Biol *15*, e2003268.

643   19.   Grosshans, J., and Wieschaus, E. (2000). A genetic link between morphogenesis and
644   cell division during formation of the ventral furrow in Drosophila. Cell *101*, 523-531.
645   20.   Hahn, A.T., Jones, J.T., and Meyer, T. (2009). Quantitative analysis of cell cycle phase
646   durations and PC12 differentiation using fluorescent biosensors. Cell Cycle *8*, 1044-1052.
647   21.   Halevy, O., Novitch, B.G., Spicer, D.B., Skapek, S.X., Rhee, J., Hannon, G.J., Beach,
648   D., and Lassar, A.B. (1995). Correlation of terminal cell cycle arrest of skeletal muscle with
649   induction of p21 by MyoD. Science *267*, 1018-1021.
650   22.   Halloran, M.C., Sato-Maeda, M., Warren, J.T., Su, F., Lele, Z., Krone, P.H., Kuwada,
651   J.Y., and Shoji, W. (2000). Laser-induced gene expression in specific cells of transgenic
652   zebrafish. Development *127*, 1953-1960.
653   23.   Hartwell, L.H., Culotti, J., Pringle, J.R., and Reid, B.J. (1974). Genetic control of the cell
654   division cycle in yeast. Science *183*, 46-51.
655   24.   Hintze, M., Koneru, S.L., Gilbert, S.P.R., Katsanos, D., Lambert, J., and Barkoulas, M.
656   (2020). A Cell Fate Switch in the Caenorhabditis elegans Seam Cell Lineage Occurs Through
657   Modulation of the Wnt Asymmetry Pathway in Response to Temperature Increase. Genetics
658   *214*, 927-939.
659   25.   Hong, Y., Roy, R., and Ambros, V. (1998). Developmental regulation of a cyclin-
660   dependent kinase inhibitor controls postembryonic cell cycle progression in Caenorhabditis
661   elegans. Development *125*, 3585-3597.
662   26.   Hsu, C.H., Altschuler, S.J., and Wu, L.F. (2019). Patterns of Early p21 Dynamics
663   Determine Proliferation-Senescence Cell Fate after Chemotherapy. Cell *178*, 361-373 e312.
664   27.   Hur, W., Kemp, J.P., Jr., Tarzia, M., Deneke, V.E., Marzluff, W.F., Duronio, R.J., and Di
665   Talia, S. (2020). CDK-Regulated Phase Separation Seeded by Histone Genes Ensures Precise
666   Growth and Function of Histone Locus Bodies. Dev Cell.
667   28.   Jones, S.M., and Kazlauskas, A. (2001). Growth-factor-dependent mitogenesis requires
668   two distinct phases of signalling. Nat Cell Biol *3*, 165-172.
669   29.   Katsanos, D., Koneru, S.L., Mestek Boukhibar, L., Gritti, N., Ghose, R., Appleford, P.J.,
670   Doitsidou, M., Woollard, A., van Zon, J.S., Poole, R.J.*, et al.* (2017). Stochastic loss and gain of
671   symmetric divisions in the C. elegans epidermis perturbs robustness of stem cell number. PLoS
672   Biol *15*, e2002429.
673   30.   Katz, W.S., Hill, R.J., Clandinin, T.R., and Sternberg, P.W. (1995). Different levels of the
674   C. elegans growth factor LIN-3 promote distinct vulval precursor fates. Cell *82*, 297-307.
675   31.   Kocsisova, Z., Kornfeld, K., and Schedl, T. (2018). Cell cycle accumulation of the
676   proliferating cell nuclear antigen PCN-1 transitions from continuous in the adult germline to
677   intermittent in the early embryo of C. elegans. BMC Dev Biol *18*, 12.
678   32.   Kohrman, A.Q., and Matus, D.Q. (2017). Divide or Conquer: Cell Cycle Regulation of
679   Invasive Behavior. Trends Cell Biol *27*, 12-25.
680   33.   Leise, W.F., 3rd, and Mueller, P.R. (2004). Inhibition of the cell cycle is required for
681   convergent extension of the paraxial mesoderm during Xenopus neurulation. Development *131*,
682   1703-1715.
683   34.   Leung, B., Hermann, G.J., and Priess, J.R. (1999). Organogenesis of the Caenorhabditis
684   elegans intestine. Dev Biol *216*, 114-134.
685   35.   Martin, B.L. (2016). Factors that coordinate mesoderm specification from
686   neuromesodermal progenitors with segmentation during vertebrate axial extension. Semin Cell
687   Dev Biol *49*, 59-67.
688   36.   Matus, D.Q., Chang, E., Makohon-Moore, S.C., Hagedorn, M.A., Chi, Q.Y., and
689   Sherwood, D.R. (2014). Cell division and targeted cell cycle arrest opens and stabilizes
690   basement membrane gaps. Nature communications *5*, 13.
691   37.   Matus, D.Q., Lohmer, L.L., Kelley, L.C., Schindler, A.J., Kohrman, A.Q., Barkoulas, M.,
692   Zhang, W., Chi, Q., and Sherwood, D.R. (2015). Invasive Cell Fate Requires G1 Cell-Cycle

693 Arrest and Histone Deacetylase-Mediated Changes in Gene Expression. Developmental Cell
694 *35*, 162-174.
695 38. Medwig-Kinney, T.N., Smith, J.J., Palmisano, N.J., Tank, S., Zhang, W., and Matus,
696 D.Q. (2020). A developmental gene regulatory network for C. elegans anchor cell invasion.
697 Development *147*.
698 39. Miller, I., Min, M., Yang, C., Tian, C., Gookin, S., Carter, D., and Spencer, S.L. (2018).
699 Ki67 is a Graded Rather than a Binary Marker of Proliferation versus Quiescence. Cell Rep *24*,
700 1105-1112 e1105.
701 40. Min, M., Rong, Y., Tian, C., and Spencer, S. (2020). Temporal integration of mitogen
702 history in mother cells controls proliferation of daughter cells. Science.
703 41. Moser, J., Miller, I., Carter, D., and Spencer, S.L. (2018). Control of the Restriction Point
704 by Rb and p21. Proc Natl Acad Sci U S A *115*, E8219-E8227.
705 42. Murakami, M.S., Moody, S.A., Daar, I.O., and Morrison, D.K. (2004). Morphogenesis
706 during Xenopus gastrulation requires Wee1-mediated inhibition of cell proliferation.
707 Development *131*, 571-580.
708 43. Newport, J., and Kirschner, M. (1982). A major developmental transition in early
709 Xenopus embryos: I. characterization and timing of cellular changes at the midblastula stage.
710 Cell *30*, 675-686.
711 44. Oki, T., Nishimura, K., Kitaura, J., Togami, K., Maehara, A., Izawa, K., Sakaue-Sawano,
712 A., Niida, A., Miyano, S., Aburatani, H*., et al.* (2014). A novel cell-cycle-indicator, mVenus-p27K-
713 , identifies quiescent cells and visualizes G0-G1 transition. Sci Rep *4*, 4012.
714 45. Osborn, D.P., Li, K., Hinits, Y., and Hughes, S.M. (2011). Cdkn1c drives muscle
715 differentiation through a positive feedback loop with Myod. Dev Biol *350*, 464-475.
716 46. Overton, K.W., Spencer, S.L., Noderer, W.L., Meyer, T., and Wang, C.L. (2014). Basal
717 p21 controls population heterogeneity in cycling and quiescent cell cycle states. Proc Natl Acad
718 Sci U S A *111*, E4386-4393.
719 47. Ozpolat, B.D., Handberg-Thorsager, M., Vervoort, M., and Balavoine, G. (2017). Cell
720 lineage and cell cycling analyses of the 4d micromere using live imaging in the marine annelid
721 Platynereis dumerilii. Elife *6*.
722 48. Pardee, A.B. (1974). A restriction point for control of normal animal cell proliferation.
723 Proc Natl Acad Sci U S A *71*, 1286-1290.
724 49. Rasmussen, J.P., Feldman, J.L., Reddy, S.S., and Priess, J.R. (2013). Cell interactions
725 and patterned intercalations shape and link epithelial tubes in C. elegans. PLoS Genet *9*,
726 e1003772.
727 50. Ruijtenberg, S., and van den Heuvel, S. (2015). G1/S Inhibitors and the SWI/SNF
728 Complex Control Cell-Cycle Exit during Muscle Differentiation. Cell.
729 51. Sakaue-Sawano, A., Kurokawa, H., Morimura, T., Hanyu, A., Hama, H., Osawa, H.,
730 Kashiwagi, S., Fukami, K., Miyata, T., Miyoshi, H*., et al.* (2008). Visualizing Spatiotemporal
731 Dynamics of Multicellular Cell-Cycle Progression. Cell *132*, 487-498.
732 52. Schwarz, C., Johnson, A., Koivomagi, M., Zatulovskiy, E., Kravitz, C.J., Doncic, A., and
733 Skotheim, J.M. (2018). A Precise Cdk Activity Threshold Determines Passage through the
734 Restriction Point. Molecular cell *69*, 253-264 e255.
735 53. Shoji, W., Yee, C.S., and Kuwada, J.Y. (1998). Zebrafish semaphorin Z1a collapses
736 specific growth cones and alters their pathway in vivo. Development *125*, 1275-1283.
737 54. Spencer, S.L., Cappell, S.D., Tsai, F.C., Overton, K.W., Wang, C.L., and Meyer, T.
738 (2013). The proliferation-quiescence decision is controlled by a bifurcation in CDK2 activity at
739 mitotic exit. Cell *155*, 369-383.
740 55. Sternberg, P.W. (1984). Control of cell lineage during nematode development
741 (Cambridge, MA: Massachusetts Institute of Technology).
742 56. Sternberg, P.W., and Horvitz, H.R. (1986). Pattern formation during vulval development
743 in C. elegans. Cell *44*, 761-772.

744   57.   Strzyz, P.J., Lee, H.O., Sidhaye, J., Weber, I.P., Leung, L.C., and Norden, C. (2015).
745   Interkinetic nuclear migration is centrosome independent and ensures apical cell division to
746   maintain tissue integrity. Dev Cell *32*, 203-219.
747   58.   Sugiyama, M., Saitou, T., Kurokawa, H., Sakaue-Sawano, A., Imamura, T., Miyawaki,
748   A., and Iimura, T. (2014). Live imaging-based model selection reveals periodic regulation of the
749   stochastic G1/S phase transition in vertebrate axial development. PLoS Comput Biol *10*,
750   e1003957.
751   59.   Sugiyama, M., Sakaue-Sawano, A., Iimura, T., Fukami, K., Kitaguchi, T., Kawakami, K.,
752   Okamoto, H., Higashijima, S., and Miyawaki, A. (2009). Illuminating cell-cycle progression in the
753   developing zebrafish embryo. Proc Natl Acad Sci U S A *106*, 20812-20817.
754   60.   Sulston, J.E., and Horvitz, H.R. (1977). Post-embryonic cell lineages of the nematode,
755   Caenorhabditis elegans. Dev Biol *56*, 110-156.
756   61.   Sun, D., and Buttitta, L. (2017). States of G0 and the proliferation-quiescence decision in
757   cells, tissues and during development. Int J Dev Biol *61*, 357-366.
758   62.   Tomura, M., Sakaue-Sawano, A., Mori, Y., Takase-Utsugi, M., Hata, A., Ohtawa, K.,
759   Kanagawa, O., and Miyawaki, A. (2013). Contrasting quiescent G0 phase with mitotic cell
760   cycling in the mouse immune system. PLoS One *8*, e73801.
761   63.   van der Horst, S.E.M., Cravo, J., Woollard, A., Teapal, J., and van den Heuvel, S.
762   (2019). C. elegans Runx/CBFbeta suppresses POP-1 TCF to convert asymmetric to
763   proliferative division of stem cell-like seam cells. Development *146*.
764   64.   van Rijnberk, L.M., van der Horst, S.E., van den Heuvel, S., and Ruijtenberg, S. (2017).
765   A dual transcriptional reporter and CDK-activity sensor marks cell cycle entry and progression in
766   C. elegans. PLoS One *12*, e0171600.
767   65.   Yang, H.W., Chung, M., Kudo, T., and Meyer, T. (2017). Competing memories of
768   mitogen and p53 signalling control cell-cycle entry. Nature *549*, 404-408.
769   66.   Yang, R., and Feldman, J.L. (2015). SPD-2/CEP192 and CDK Are Limiting for
770   Microtubule-Organizing Center Function at the Centrosome. Curr Biol *25*, 1924-1931.
771   67.   Yang, Z.J., Broz, D.K., Noderer, W.L., Ferreira, J.P., Overton, K.W., Spencer, S.L.,
772   Meyer, T., Tapscott, S.J., Attardi, L.D., and Wang, C.L. (2015). p53 suppresses muscle
773   differentiation at the myogenin step in response to genotoxic stress. Cell Death Differ *22*, 560-
774   573.
775   68.   Zerjatke, T., Gak, I.A., Kirova, D., Fuhrmann, M., Daniel, K., Gonciarz, M., Muller, D.,
776   Glauche, I., and Mansfeld, J. (2017). Quantitative Cell Cycle Analysis Based on an Endogenous
777   All-in-One Reporter for Cell Tracking and Classification. Cell Rep *19*, 1953-1966.
778   69.   Zetterberg, A., and Larsson, O. (1985). Kinetic analysis of regulatory events in G1
779   leading to proliferation or quiescence of Swiss 3T3 cells. Proc Natl Acad Sci U S A *82*, 5365-
780   5369.
781   70.   Ziel, J.W., Hagedorn, E.J., Audhya, A., and Sherwood, D.R. (2009). UNC-6 (netrin)
782   orients the invasive membrane of the anchor cell in C. elegans. Nature Cell Biology *11*, 183-
783   189.
784   71.   Zielke, N., and Edgar, B.A. (2015). FUCCI sensors: powerful new tools for analysis of
785   cell proliferation. Wiley Interdiscip Rev Dev Biol *4*, 469-487.
786   72.   Zwang, Y., Sas-Chen, A., Drier, Y., Shay, T., Avraham, R., Lauriola, M., Shema, E.,
787   Lidor-Nili, E., Jacob-Hirsch, J., Amariglio, N.*, et al.* (2011). Two phases of mitogenic signaling
788   unveil roles for p53 and EGR1 in elimination of inconsistent growth signals. Molecular cell *42*,
789   524-535.
790
791
792
793
794
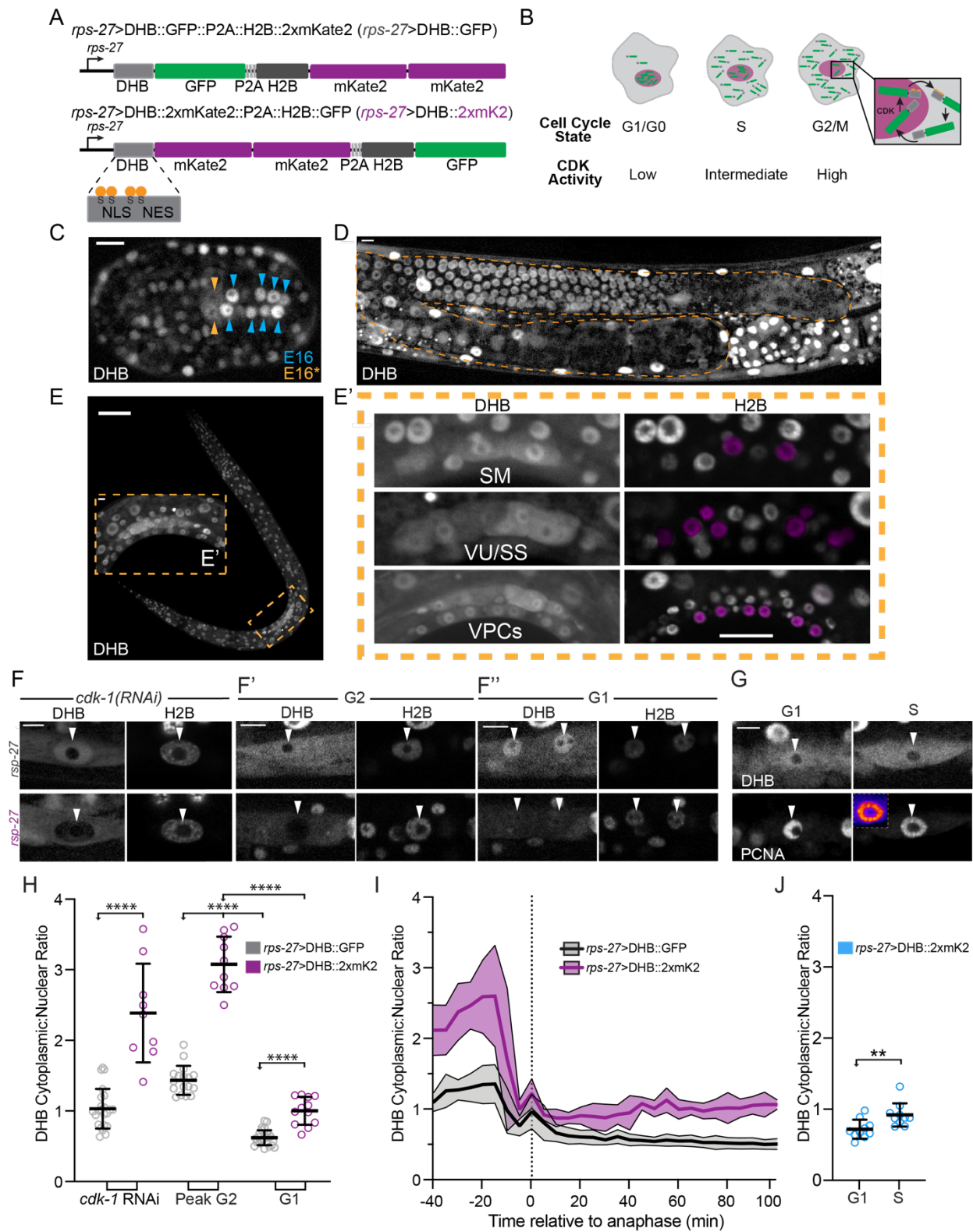
799

Figure 1. Generation of a CDK sensor for live cell cycle visualization in *C. elegans*. (A) Schematic of CDK sensor fused to GFP (top) or two copies of mKate2 (bottom) and a nuclear mask (H2B::FP) separated by a self-cleaving peptide (P2A). Inset: nuclear-localization signal (NLS), nuclear export signal (NES), CDK consensus phosphorylation sites on serine (S). (B) Schematic of CDK sensor translocation during the cell cycle. (C) Quiescent E16 cells (blue arrows) versus the cycling E16* star cells (orange) arrows. (D-E) Confocal micrograph montage of CDK sensor in the *C. elegans* germline (D, orange dashed line) and L3 stage larvae (E). Three somatic tissues are highlighted (inset, dashed orange box) shown at higher magnification in E', with pseudo colored nuclei (magenta) depicting cells of interest. (F, G) Representative images of sensor expression in SM cells following *cdk-1* RNAi treatment; at peak G2 (F') and 20 minutes after anaphase during G1 (F'') in DHB::GFP (grey) and DHB::2xmKate2 (magenta) and DHB::2xmKate2 co-expressed with PCNA (*pcn-1*>PCN-1::GFP), inset highlights PCNA puncta in S phase. (H) Dot plot depicting dynamic ranges of the two CDK sensor variants, measured by the cytoplasmic:nuclear ratio of DHB mean fluorescent intensity, at the peak of G_2 and G_1 in the SMs ($n \geq 9$). (I) Plot of DHB cytoplasmic:nuclear ratio in SM cells during one round of cell division, measured every 5 minutes ($n=4$ per strain). Dotted line indicates time of anaphase. Error bars and shaded error bands depict mean±standard deviation. (J) Dot plot depicting range of G1 and S phase in DHB::2xmKate2 based on PCNA localization ($n \geq 7$ per strain). ** $p \leq 0.01$, ****$p \leq 0.0001$ Significance as determined by statistical simulation; exact *p*-values in **Table S1**. Scale bar = 10 µm except in (E; 20 µm and F; 5 µm).

820
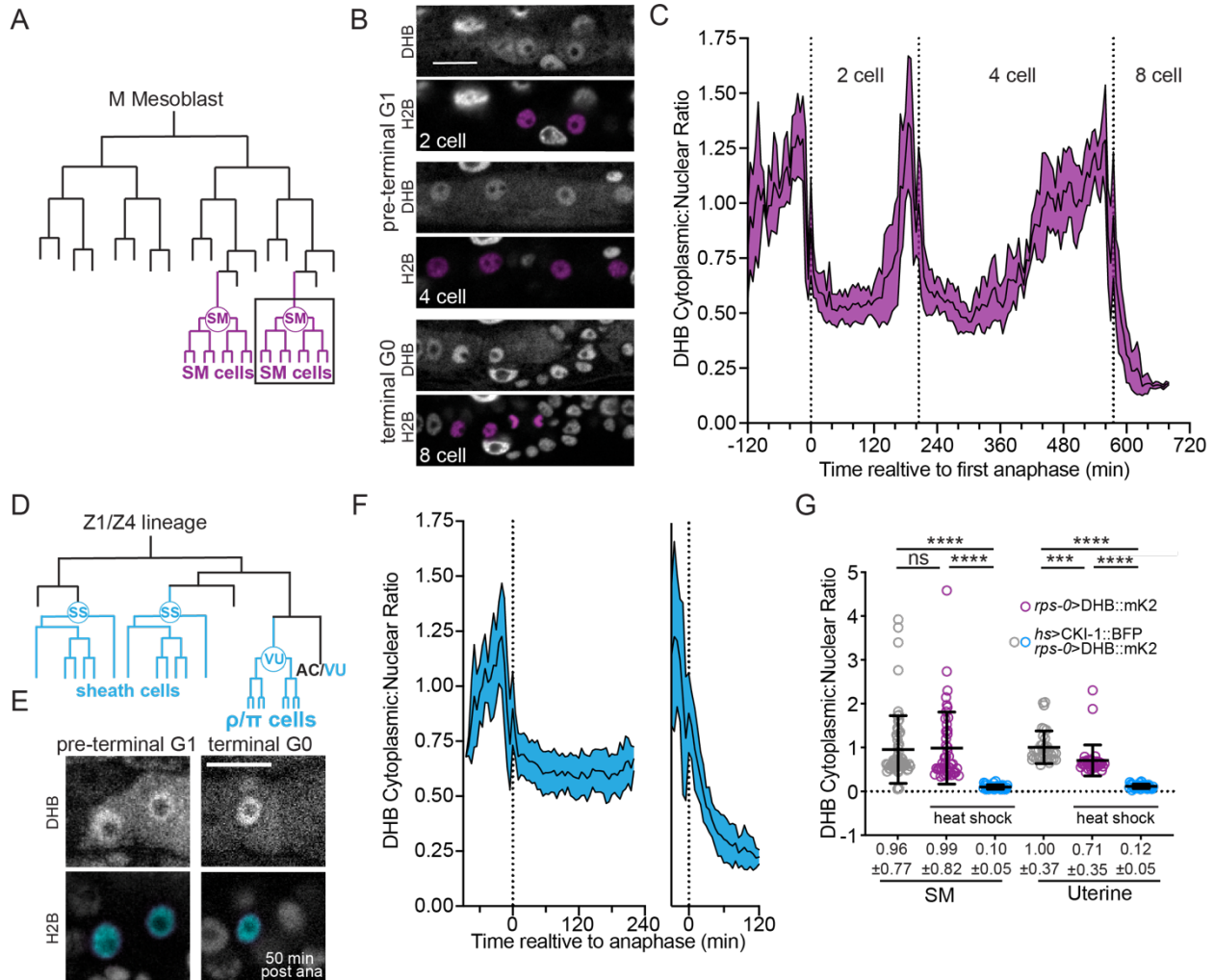
Figure 2. Sex myoblasts and somatic gonad cells exit terminal divisions into a CDK^{low} state. SM (A) and uterine (D) lineage schematics. (B) Micrographs of a time-lapse movie showing SM cells (B) and uterine cells (E) at G$_1$ in pre-terminal divisions and G$_0$ upon terminal differentiation. Quantification of CDK sensor in SM cells (C; $n{\geq}10$) and uterine cells (F; $n{\geq}13$). (G) Quantification of CDK sensor localization in SM cells and uterine cells following ectopic expression of CKI-1 (*hsp*>CKI-1::2xmTagBFP2) compared to non-heat shock controls and heat shock animals without the inducible transgene ($n{\geq}36$ per treatment). Scale bars = 10 μm. Pseudo colored nuclei (magenta, B; cyan, E) indicate cells of interest. Dotted line indicates time of anaphase. Line and shaded error bands depict mean ± standard deviation, time series measured every 5 minutes. ****p≤0.0001 Significance as determined by statistical simulations; *p*-values in **Table S1**.

23

837
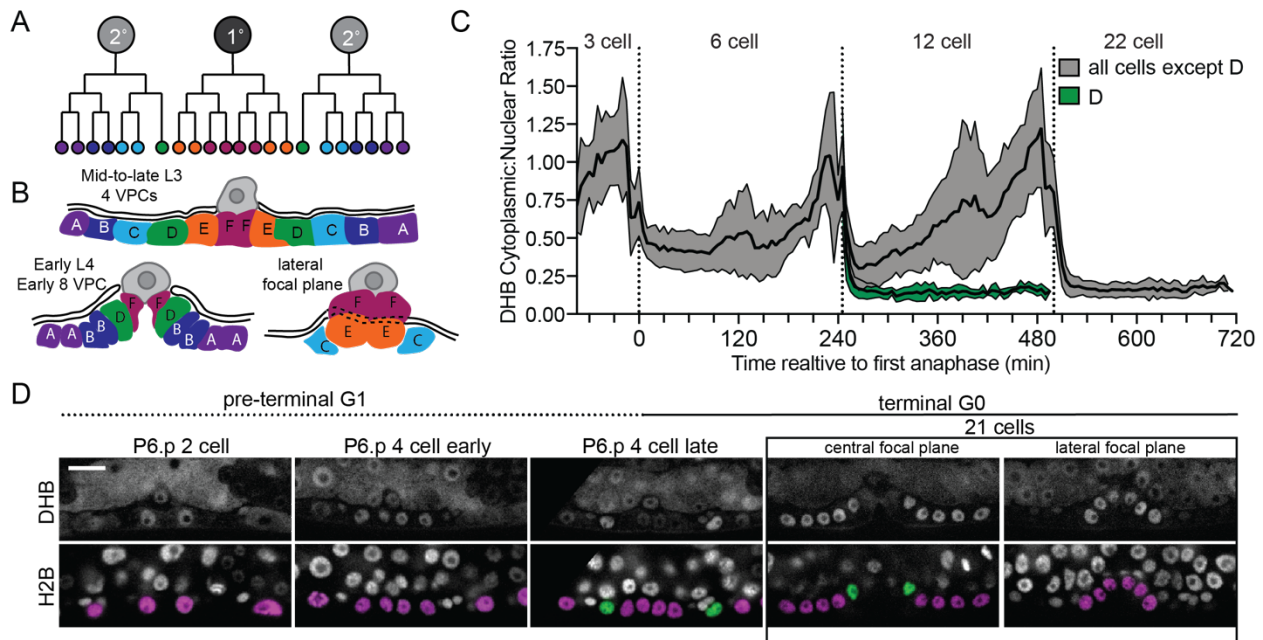
Figure 3. Vulval precursor cells exit terminal divisions into a CDK^{low} state. (A) Schematic of primary (1°) and secondary (2°) fated vulval precursor cells (VPCs). (B) All of the VPCs, with the exception of the D cells, divide to facilitate vulval morphogenesis. (C) Time series of CDK sensor localization in the 1° and 2° VPCs, as measured every 5 min. Note that the terminally differentiated D cells are born into a CDK^{low} state ($n \geq 9$). Dotted line indicates time of anaphase. Shaded error bands depict mean±standard deviation. (D) Representative images of CDK sensor localization in the VPCs from the P6.p 2-cell stage to 8-cell stage. Nuclei (H2B) are highlighted in magenta for non-D cell 1° and 2° VPCs and green for the D cells. Scale bar = 10 μm.
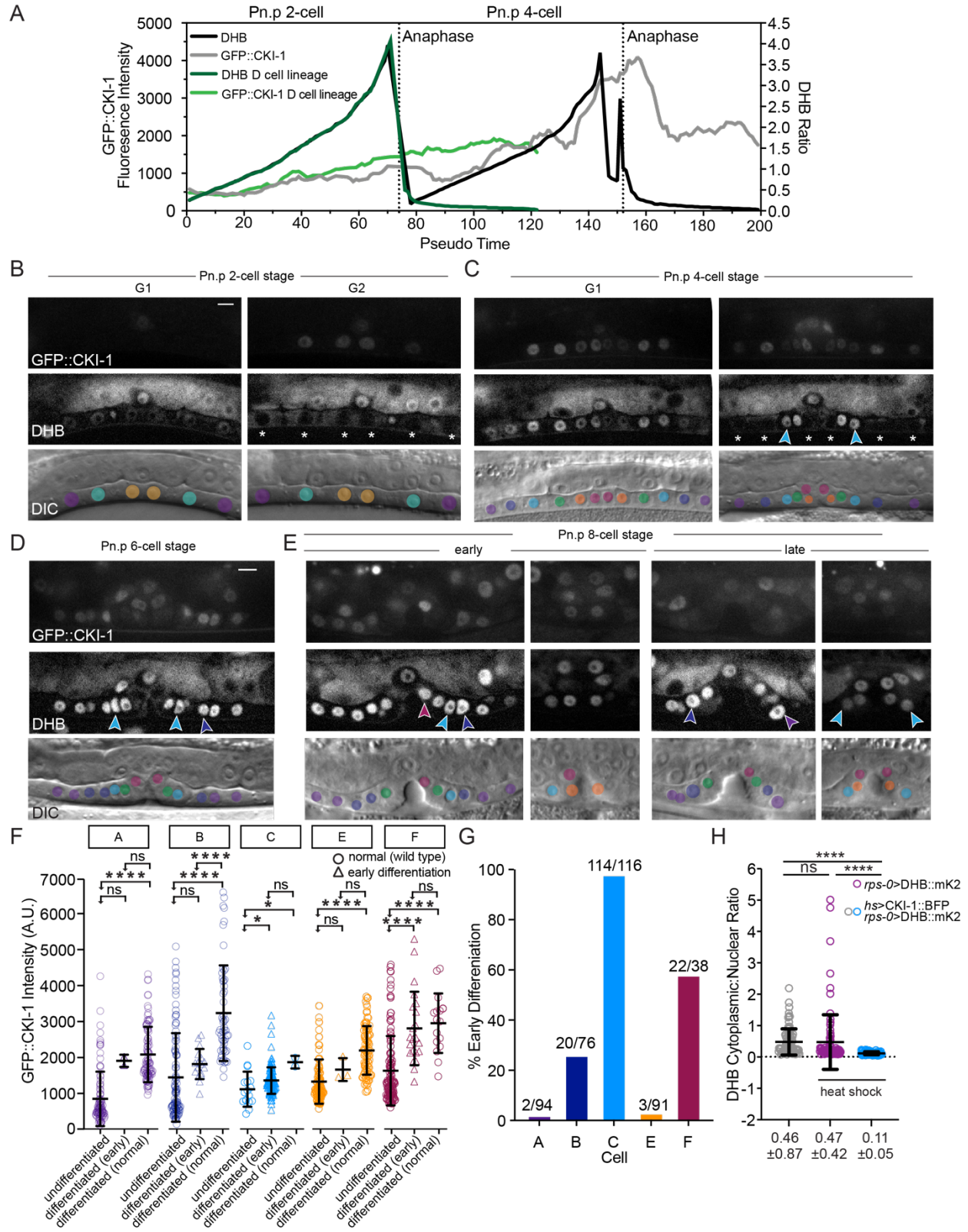
853 **Figure 4. CKI-1 levels peak prior to terminal differentiation.** (A) CDK sensor activity and CKI-
854 1 levels across pseudo-time, DHB ratios for all VPCs (black line) and D cells (dark green line).
855 GFP::CKI-1 fluorescence intensity in VPCs (grey line) and D cell (light green line). (B)
856 Representative images of VPCs at the Pn.p 2-cell stage at G_1 and G_2 (white asterisk). (C)
857 Representative images of VPCs at the Pn.p 4-cell stage at G_1 and G_2; early differentiated C cells
858 (cyan arrows) with low levels of GFP::CKI-1. (D-E) Representative images of VPCs at the Pn.p
859 6-cell stage (D) and 8-cell stage (E); arrows show early differentiated C (cyan) and B cell (dark
860 blue), F cell (magenta arrow), and A cell (purple arrow). (F) GFP::CKI-1 fluorescence intensity in
861 each cell of the VPC lineage. (G) Percentage of cells of each lineage that showed early
862 differentiation and did not undergo their final division. (H) Overexpression of CKI-1 via heat shock
863 causes pre-terminally differentiated cells to enter G_0 state. Scale bar = 10 µm. *p≤0.05,
864 ****p≤0.0001 Significance as determined by statistical simulations; *p*-values in **Table S1**.
865
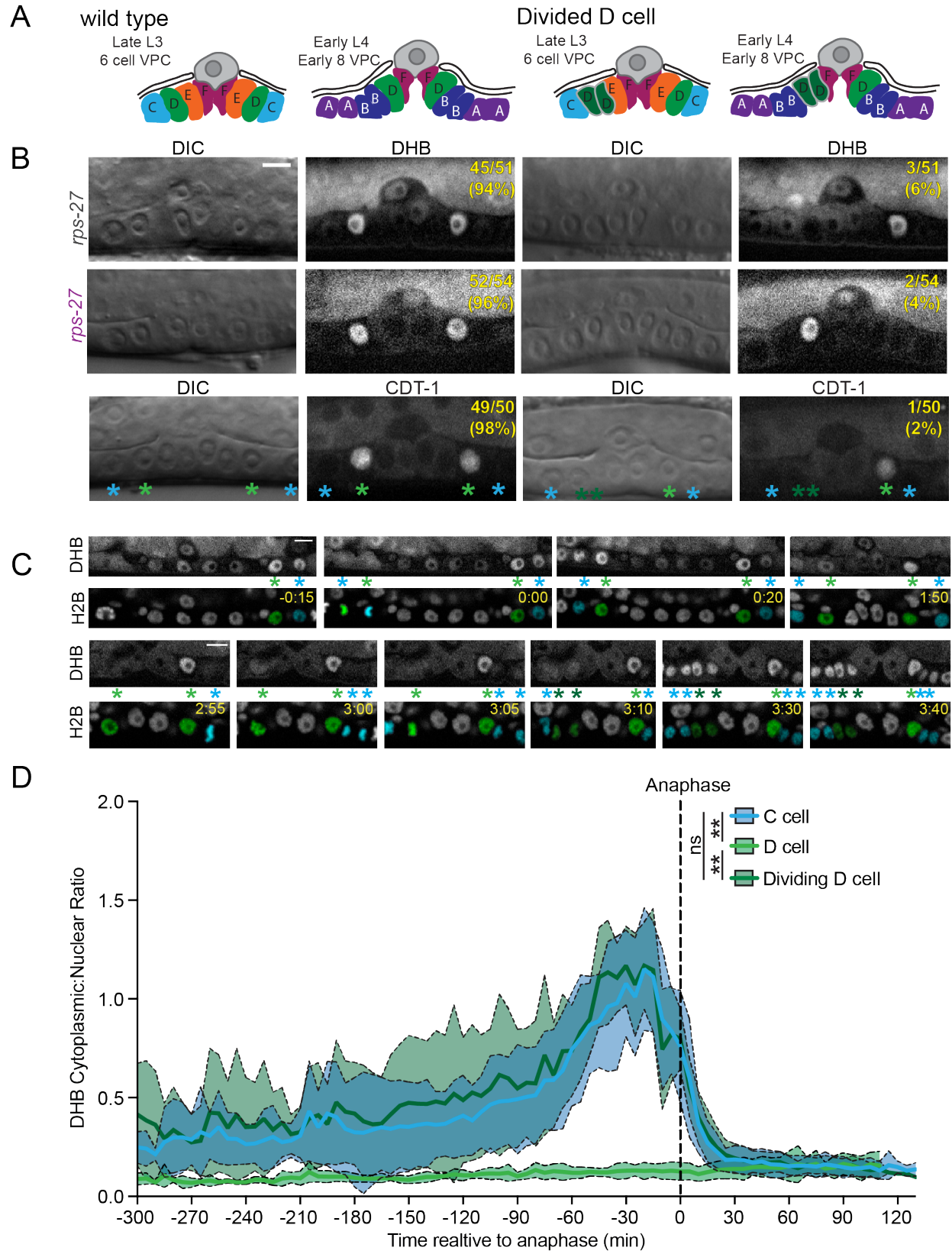
868 **Figure 5. CDK activity predicts a cryptic stochastic fate decision in an invariant cell lineage.**
869 (A) Schematic of wild type vulva and vulva with a divided D cell. (B) Representative images at the
870 Pn.p 6 cell stage from CDK sensor strains (top, middle) and endogenous *cdt-1::GFP* (bottom),
871 showing wild type vulva on the left and vulva with a divided D cell on the right. Penetrance of each
872 phenotype for each strain is annotated on the DHB image. (C) Frames from a time-lapse with a
873 dividing D cell (left) (see Movie S5). Nuclei (H2B) are highlighted in green for the D cell and cyan
874 for the C cells. (D) DHB ratio for C cell, terminally differentiated D cell and dividing D cell. Dotted
875 line indicates time of anaphase. Line and shaded error bands depict mean±standard deviation.
876 Green asterisks or pseudo colored nuclei mark the D cell and cyan asterisks or pseudo colored
877 nuclei mark the C cell, scale bar = 10 μm. ** p≤0.01, *P* values determined Significance as
878 determined by statistical simulations; *p*-values in **Table S1**.
879
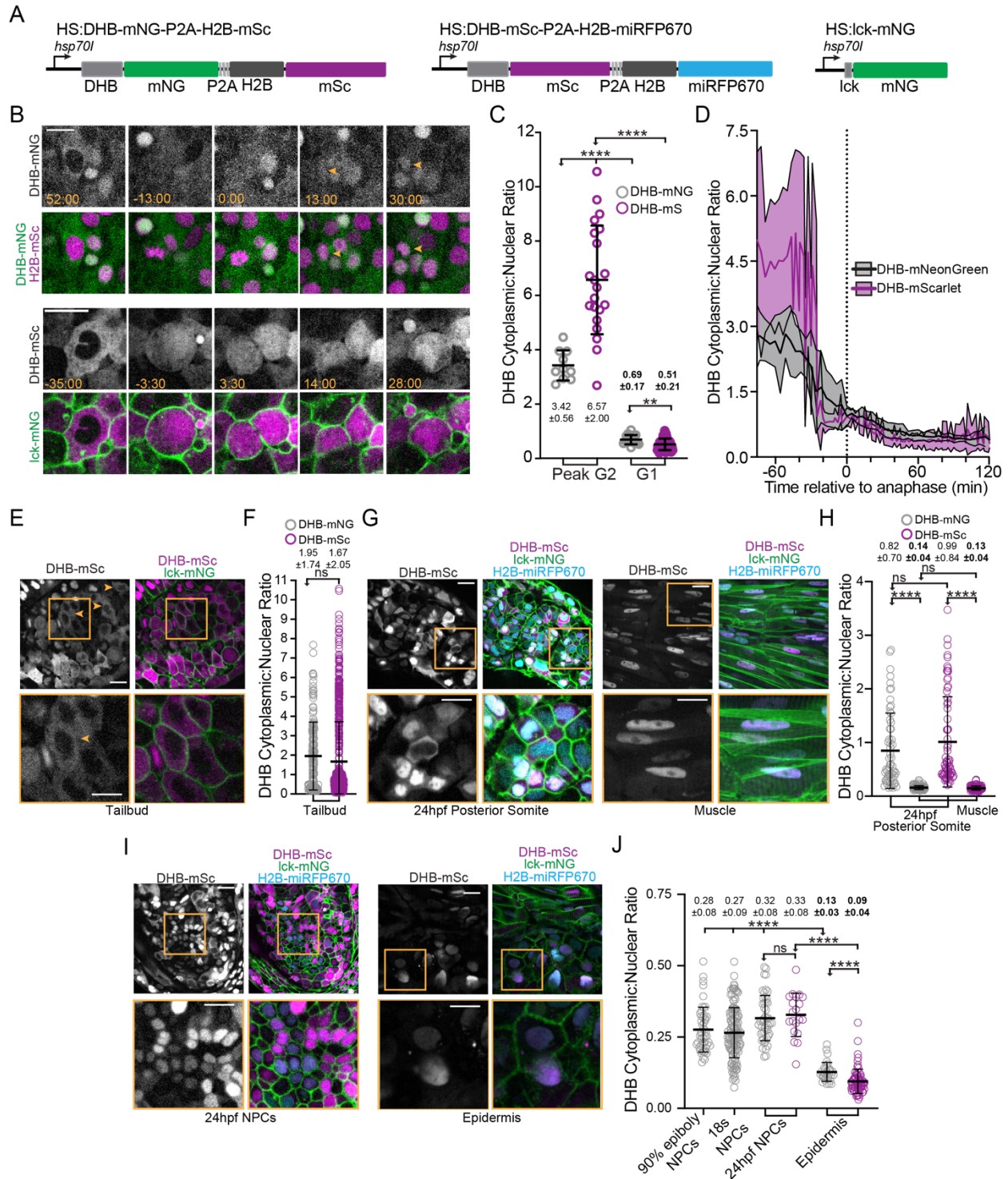
880

881 **Figure 6. Generation of inducible CDK sensor transgenic lines in the zebrafish.** (A)
882 Schematics of inducible zebrafish variants of the CDK sensor fused to mNG (left) or mSc (middle)
883 and a nuclear mask (H2B::FP) separated by a self-cleaving peptide (P2A). Schematic of inducible
884 membrane marker (lck-mNG; right). (B-D) Frames (B), dot plot (C) and DHB ratio plot (D) from
885 time lapse of DHB-mNG (top, gray) and DHB-mSc (bottom, magenta) of peak G_2 through
886 anaphase and G_1 (n>10 examined for each). Dotted line indicates time of anaphase. (E-F)

29

887   Representative micrographs of CDK sensor (E, orange arrows and box inset highlights cytosolic
888   CDK sensor localization) and quantification of DHB ratio (F) in the tailbud. (G-J) Representative
889   micrographs (G, I) and quantification of DHB ratios (H, J) in cells of 24 hpf posterior somites and
890   terminally differentiated muscle at 72 hpf (G), notochord progenitors (NPCs) and epidermis at 72
891   hpf (I). Insets, orange box, Scale bar = 20 μm. Line and error bars depict mean±standard
892   deviation, numbers in **bold** are tissues in G_0. ** p≤0.01, ****p≤0.0001 *P* values determined by
893   statistical simulations, exact values reported in **Table S1**.
894
895
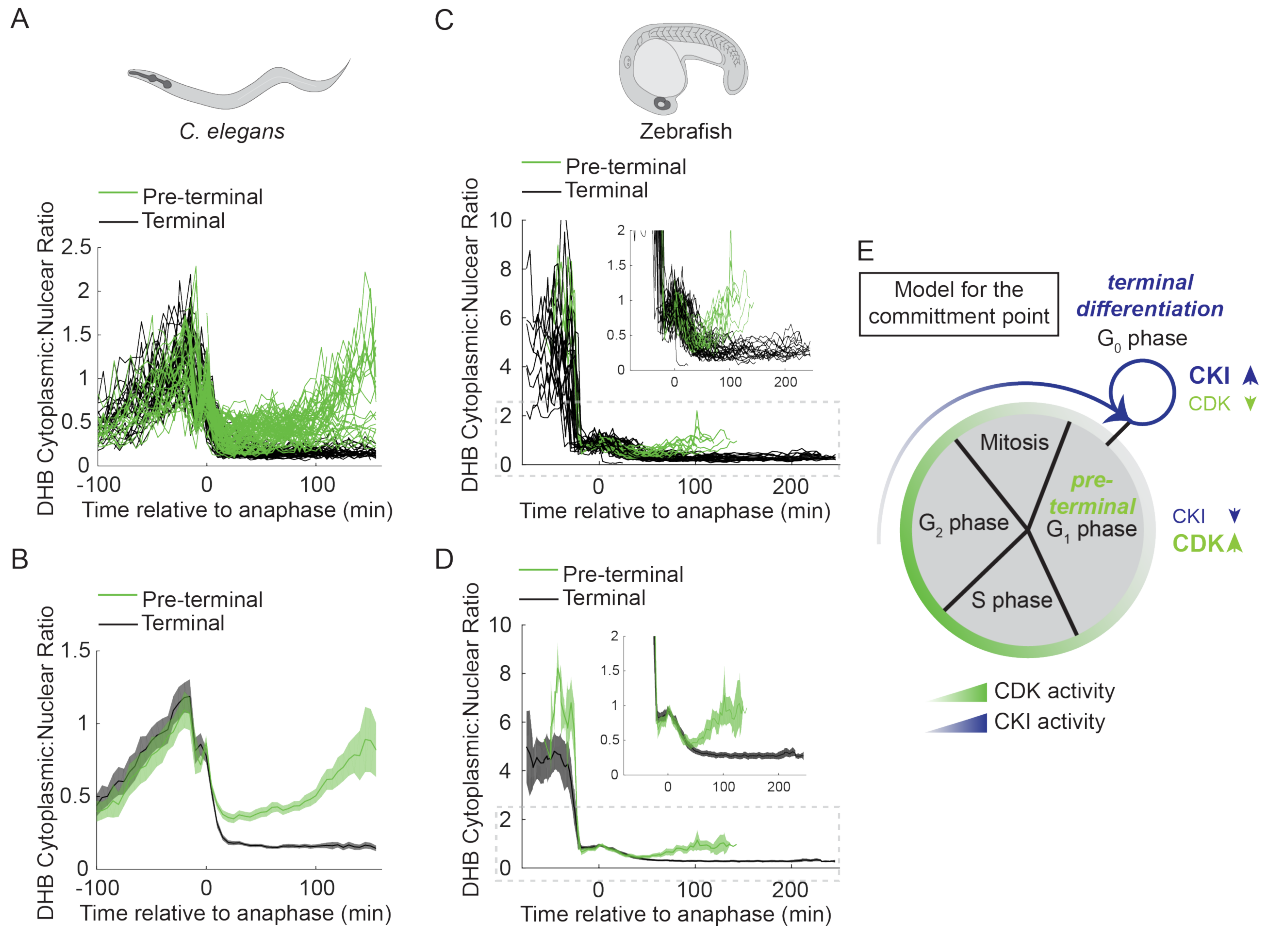
Figure 7. A bifurcation in CDK activity at mitotic exit controls the proliferation-differentiation decision. (A-D) Single-cell traces of CDK activity for all quantified *C. elegans* (A-B) and zebrafish (C-D) cell births for CDK^{inc} cells (green) and CDK^{low} cells (black). DHB ratio of single-cell data (A, C) and mean±95% confidence interval (B, D) are plotted for each cell analyzed relative to anaphase. (E) A model for the metazoan commitment point argues that the G_1/G_0 decision is influenced by a maternal input of CKI activity and that CDK activity shortly after mitotic exit determines future cell fate.